1  **Internal tides off the Amazon shelf in the western tropical Atlantic: Analysis of**
2  **SWOT Cal/Val Mission Data**

3  Michel Tchilibou[1], Loren Carrere[1], Florent Lyard[2], Clément Ubelmann[3], Gérald Dibarboure[4] ,
4  Edward D. Zaron[5], and Brian K. Arbic[6]

5  [1] Collecte Localisation Satellites, 31520 Ramonville-Saint-Agne, France

6  [2] Université de Toulouse, LEGOS (CNES/CNRS/IRD/UT3), 31400 Toulouse, France

7  [3] Datlas, Grenoble, France

8  [4] Centre National d'Etude Spatiales, 31400, Toulouse, France

9  [5] College of Earth, Ocean and Atmospheric Science, Oregon State University, Corvallis, OR, USA

10  [6] Department of Earth and Environmental Sciences, University of Michigan, Ann Arbor, MI, USA

11  Correspondence to: Michel Tchilibou (mtchilibou@groupcls.com)

12  **Abstract**

13  This study focuses on the internal tides (IT) off the Amazon shelf in the tropical Atlantic. It is based
14  on 2 km horizontally gridded observations along the swaths of SWOT (Surface Water and Ocean
15  Topography) track 20 during the calibration/validation phase (Cal/Val, 1-day orbit) from late March to
16  early July 2023. We evaluate the amplitude of $M_2$, $N_2$ and $S_2$ frequencies and use the $M_2$ atlas as an
17  internal tide correction model for SWOT observations. Internal tide amplitudes (models or atlases) are
18  first derived by harmonic analysis of the SWOT sea level anomaly (SLA). The estimation is improved by
19  performing a principal component analysis (PCA) before the harmonic analysis. The results compare
20  very well with the high-resolution empirical tide (HRET) internal tide model, the reference product for
21  internal tide corrections in altimetry observations.  The coherent mode 1 and mode 2 $M_2$ tides can be
22  distinguished in the internal tide model derived from SWOT, while the higher modes with their strong
23  SLA signature are seen mostly in the incoherent part.  In comparison to HRET, the correction of SWOT
24  observations with SWOT-based atlases may be more relevant for this track.

25  **Introduction**

26  The launch of the SWOT mission at the end of 2022 certainly marks a new phase in spatial altimetry.
27  SWOT is equipped with the KaRIn instrument, a Ka-band radar interferometer capable of measuring
28  the sea surface topography with unprecedented resolution in two-dimensional swaths. KaRIn consists
29  of two antennae that take 2D measurements in two 50 km-wide swaths  separated by a 20 km gap
30  covered by the conventional nadir radar altimeter also carried by the mission. The accuracy of SWOT's
31  instruments is such that SWOT should be able to observe the ocean down to a spatial scale of 15-30
32  km (Morrow et al., 2019; Dufau et al., 2016; Wang et al., 2019), thus, complementing our 2D view of
33  the ocean with Topex/Poseidon class nadir altimetry, which is limited to scales larger than 150 km
34  (Chelton et al., 2011; Ballarotta et al., 2019) along one-dimensional tracks rather than two-dimensional
35  swaths. The main oceanographic objective of the SWOT mission is to characterize mesoscale and sub-
36  mesoscale ocean circulation (Fu et al., 2012; Fu and Ubelmann, 2014). However, ocean processes at
37  the scales targeted by SWOT (150-15 km) encompass both "balanced" geostrophic motions, as well as
38  surface and internal inertia-gravity waves at tidal frequencies. The correction of internal tides (IT)
39  surface signatures presents a significant challenge to the useability of SWOT data, considering that the

40 spatial scales of these waves overlap with those of balanced motions. Conversely, the exploitation of
41 SWOT data to study IT is an opportunity for learning more about these waves and quantifying their
42 impacts in the ocean.

43    Efforts have been made in recent years to map internal tides using conventional altimetry
44 observations. This was made possible by the fact that the internal tide has a SSH (Sea Surface height)
45 signature of the order of one to several centimeters (Ray and Mitchum, 1997). However, the coarse
46 sampling in both space and time of conventional altimetry is a hindrance. To derive spatially
47 continuous high-resolution maps of the internal tide SSH from the sparse altimeter sampling, Dushaw
48 (2015), Zhao et al. (2019) and Zaron (2019) used least-squares techniques to fit kinematic wave
49 solutions to nadir altimetry. Ubelmann et al., (2022) proposed jointly estimating internal tides and
50 mesoscale eddies to produce 2D maps of internal tides from conventional altimetry observations. The
51 advent of SWOT presents an opportunity to validate these internal tide maps using direct 2D
52 observations of the ocean. However, there is still some debate about the extraction of the internal
53 tidal signal along SWOT swaths.  The first objective of our study is thus to estimate the internal tidal
54 signal along the SWOT swaths. Le Guillou et al., (2021) propose a data assimilation method coupled
55 with a simple dynamical model to separate internal tides and balanced motion in SWOT data. The
56 possibility of using deep learning to access internal tide signals is raised by Wang et al. (2022). Without
57 questioning these methods, we will show that classical methods of harmonic analysis and principal
58 component analysis (PCA) can be used to obtain internal tide maps from SWOT data.

59    Following the linear theory of ocean vertical modes, internal tides can be decomposed as a sum of
60 orthogonal baroclinic modes (Gill, 1982; Kelly et al., 2016). The first modes (mode 1 and mode 2)
61 propagate over hundreds or even thousands of kilometers. Higher modes have much shorter
62 wavelengths and are likely to dissipate close to the internal tide generation site, due to their low group
63 velocity and high shear (St Laurent and Garrett, 2002; Vic et al.,2019) and therefore could barely be
64 observed in classical nadir altimetry observations.  In practice, the internal tide is separated into the
65 so-called coherent and incoherent internal tides. The coherent internal tide is the part of the internal
66 tide which remains phase-locked with the generating barotropic tide over an arbitrary period and is
67 easily obtained by harmonic analysis over the targeted period. Consequently, the residual that escapes
68 harmonic analysis constitutes the incoherent internal tide.  The amplitude, phase, and trajectory of
69 incoherent internal tide results from refraction, reflection, and advection of internal tide by the ocean
70 background circulation including eddies, currents, and stratification (Ponte and Klein, 2015; Nelson et
71 al.,2019; Buijsman et al., 2017; Dunphy et al., 2017; Dunphy and Lamb, 2014; Duda et al., 2018; Savage
72 et al., 2020; Barbot et al., 2021). The incoherency of the internal tide makes it difficult to correct for in
73 altimetry observations. In the SWOT data processing protocol (Dibarboure et al.,2024), the coherent
74 part of the internal tide is corrected using the HRET (High-Resolution Empirical Tide) model of Zaron
75 (2019). The second objective of this study thus concerns the correction of the coherent internal tide in
76 the SWOT data: between HRET (the reference model) and the internal tide estimates directly on SWOT,
77 which is most relevant for correcting the internal tide on SWOT data?

78    Like the barotropic tides, the internal tides are a mixture of long- and short-period waves, among
79 which are the main astronomical tides, such as the diurnal waves (O1, K1, P1) and the semi-diurnal
80 waves (M2, S2, N2, K2). Due to the long repeat cycles of altimetry satellites, short tidal periods are
81 aliased to longer periods (Le Provost, 2001).  The M2 tide, for example, is aliased to 62.11 days for the
82 TOPEX/Jason 10-day orbit (9.92 days precisely). With SWOT sampling, M2 is aliased to 66.02 days or
83 12.35 days (Table 1), depending on whether we consider the 21-day final science orbit or the 1-day
84 calibration/validation (Cal/Val) orbit (0.99343 days exactly). Table 1 gives an overview of the aliasing
85 periods of the main diurnal and semi-diurnal tidal frequencies on the SWOT Cal/Val orbit. Table 1 is

86  completed by the Rayleigh criterion values which provide information on the duration of the records
87  needed to separate the different waves. SWOT was maintained in its Cal/Val orbit for about 6 months,
88  providing slightly more than 3 months of usable data from March to early July 2023.  Our study is based
89  on this unprecedented 1-day orbit database and concerns observations along a single SWOT track in
90  the Atlantic Ocean.

91  **Table 1**: Period of aliasing (in days, second line) and separability following the Rayleigh criterion (in
92  days, from the third line to the end) of main tidal waves for SWOT's 1-day orbit.

|         | M2       | S2         | N2       | K2       | O1        | P1        | K1        | Sa         | Ssa    |
|---------|----------|------------|----------|----------|-----------|-----------|-----------|------------|--------|
| Periods | 12.35    | 75.60      | 8.53     | 129.01   | 12.97     | 106.94    | 258.03    | 365.26     | 182.62 |
| M2      | -------- | 14.77      | 27.55    | 13.66    | 258.03    | 13.97     | 12.97     | 12.79      | 13.25  |
| S2      | -------- | ---------- | 9.61     | 182.62   | 15.66     | 258.03    | 106.94    | 95.34      | 129.01 |
| N2      | ------- | ------- | -------- | 9.13     | 24.9      | 9.27      | 8.82      | 8.73       | 8.95   |
| K2      | -------- | ------- | -------- | -------- | 14.42     | 624.89    | 258.03    | 199.47     | 439.51 |
| O1      | ------- | -------- | -------- | ------- | --------- | 14.77     | 13.66     | 13.45      | 13.97  |
| P1      | ------- | -------- | -------- | ------- | -------- | --------- | 182.62    | 151.20     | 258.03 |
| K1      | ------- | -------- | -------- | ------- | ------ | -------- | --------- | 878.92     | 624.89 |
| Sa      | -------- | -------- | -------- | ------ | -------- | ------- | ----- | ---------- | 365.22 |

93

94      This study focuses on the Cal/Val track 20 off the Amazon shelf in the western tropical Atlantic
95  between 2°S and 15°N (Figure 1). The track has been chosen because the Amazon shelf is one of the
96  hot spots for internal tide generation in the ocean (Arbic et al., 2012; Solano et al. 2023; Niwa and
97  Hibiya et al., 2011). The region is marked by strong seasonal cycles of stratification, circulation and
98  eddies that regulate the generation and propagation of internal tides (Barbot 2021, Tchilibou et al.,
99  2022).  The stratification is modulated by freshwater inflows from precipitation (under the inter-
100 tropical convergence zone) and rivers (Amazon and Para rivers). The strong western boundary current,
101 the North Brazil Current (NBC), controls the extension of the Amazon's plume and develops a double
102 retroflexion into the Equatorial UnderCurrent (EUC, around 2°S-2°N) and the North Equatorial
103 CounterCurrent (NECC, around 5°N-8°N). The barotropic and baroclinic instabilities of these currents
104 generate some of the eddies present in the region (Aguedjou et al., 2019). Internal tides generated
105 between the isobaths 100 and 2000 m along the shelf break propagate mainly from the six sites
106 indicated in Figure 1 (Tchilibou et al.,2022; Assene et al., 2024).  Between March and July, the
107 pycnocline is shallow, the mesoscale activity and currents are low, consequently, internal tides tend to
108 keep more coherent (Tchilibou et al., 2022). During the rest of the year, the pycnocline is deeper,
109 mesoscale and currents are strong, and, consequently, the incoherence of internal tides increases as
110 their reflection and advection by the circulation intensifies. As they evolve, internal tides disintegrate
111 into nonlinear internal solitary waves (Jackson et al., 2012; Alford et al., 2015; Egbert and Erofeeva
112 2021). Packets of nonlinear internal solitary waves (ISWs) have been reported along the Amazon
113 continental shelf and offshore (Lentini et al., 2016; Bai et al., 2021, Brandt et al., 2002; Magalhães et
114 al., 2016). They are highly active in the area (4-8°N /40-45°W, see Figure 2 of de Macedo et al., 2023)
115 of concentration of internal tides rays emanating from sites A and D, and they have a seasonal cycle of
116 occurrence and wavelengths in agreement with those of internal waves (de Macedo et al., 2023).
117

118     The orientation of SWOT track 20 in this part of the ocean is such that it intersects three areas with
119 potentially different dynamics (Tchilibou et al., 2022). Between 2.5°S and 2.5°N (area 1, Figure 1), the
120 track is in the path of internal tides generated at points B, C and, to a lesser extent, A.  In area 2,
121 between 2.5°N and 8°N (Figure 1), the track crosses the zone of interaction between internal tides and
122 mesoscale. Finally, area 3, north of 10°N (Figure 1), lies on the mid-Atlantic Ridge, where some IT can
123 likely be generated also.  We will keep all this in mind when interpreting our results.

124      The paper is structured as follows: The data used, the evidence for the presence of internal tides in
125    the SWOT data and the variability of the SLA at different scales are presented in section 1. The
126    amplitude of the internal tides is first estimated from the SWOT data in section 2. In section 3, the
127    estimation of internal tides is improved by introducing PCA. The SWOT based internal tide models and
128    HRET are further compared in section 4. The paper ends with a conclusion and discussion.
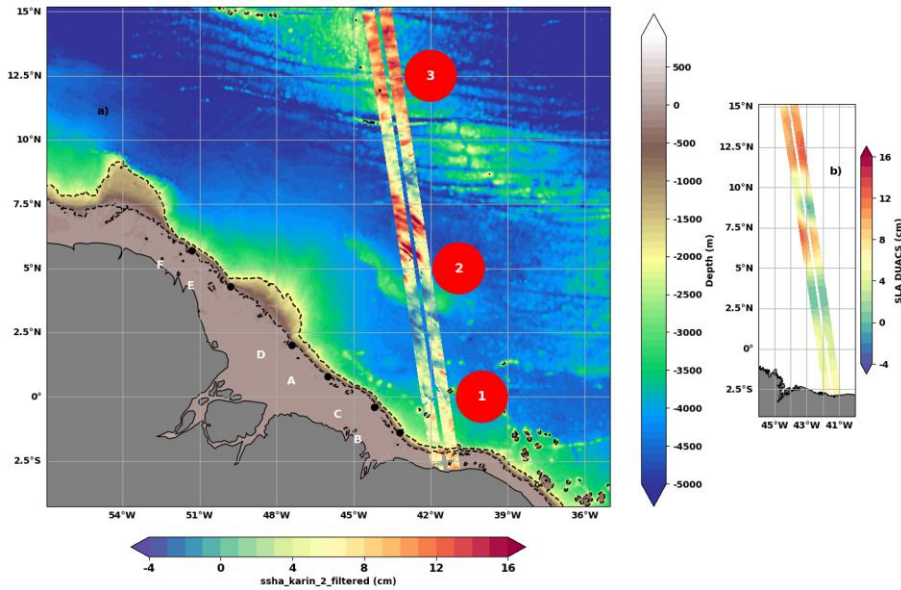


130    **Figure 1**: a) Bathymetry (m) off the Amazon shelf in the western tropical Atlantic. SLA KaRin (cm) on
131    08 April, 2023, along track 20 of SWOT's 1-day cycle. The main internal tide generation sites are marked
132    by the letters A to F. The 200 and 2000 m isobaths are dotted. The circles locate area 1 (2.5°S to 2.5°N),
133    area 2 (2.5°N to 8°N) and area 3 (north of 10°N) along the track. b) large scale structure from DUACS
134    at the same date.

135    **1- Data and Variability: Evidence of IT propagation at different scales**

136    **1.1- Description of the database:**

137    We use version V0.3 of the L3 SWOT products, released in December 2023. The data, made up of
138    several variables, are provided on regular horizontal grids of 2 km by 2 km. Using the naming
139    convention used in the dataset, we have defined the SLA by equation 1 below:

140         SLA = ssha_karin_2_filtered+ internal_tide_hret - duacs_ssha_karin_2_oi,          (1)

141    The first term on the right, 'ssha_karin_2_filtered' (the same as ssha_noiseless), is the SWOT
142    observation at the two KaRin swaths only. We exclude SWOT nadir observations, to focus on the
143    SWOT's potential to observe directly 2D maps of the ocean. The ssha_karin_2_filtered has been
144    denoised using data-driven machine-learning noise reduction and corrected from all the classic
145    physical, instrumental and environmental corrections applied in altimetry (Dibarboure et al. 2024). The
146    tidal corrections applied are FES2022 model (Lyard et al., personal communication; Lyard et al., 2021)

for the barotropic tide and HRET for the internal tide (Zaron, 2019). We reintroduced HRET's internal tide SSH (internal_tide_hret), so that our final SLA contains the total internal tide signal. The last term 'duacs_ssha_karin_2_oi' corresponds to the DUACS Maps of Sea Level Anomaly (MSLA) interpolated on SWOT swaths (Ballarotta et al., 2023; Ubelmann et al. 2015, 2021). It removes the large-scale ocean signals and particularly the mesoscale eddies that can mask internal waves at these latitudes. On track 20, we have the SLA from March 29 to July 10, 2023, i.e. 104 cycles with completely or partially filled swaths. We have removed the mean SLA from the entire Cal/Val mission.

We recall that HRET is an empirical estimate of the internal tides at the M2, S2, K1 and O1 frequencies. The variable internal_tide_hret in the SWOT data and HRET model in this paper refers to the HRETv8.1 version (Zaron, 2019). This version was developed by analyzing 25 years (1993-2017) of exact-repeat mission altimetry including the TOPEX/Poseidon-Jason missions, the ERS-Envisat-AltiKa missions and the GEOSAT Follow-On mission. The implementation of HRET involves a local two-dimensional Fourier analysis of the along-track data, and the determination of the coefficients of a spatial model by weighted least-squares fitting (second order polynomials fitting). The estimated tidal fields are gridded on a regular latitude-longitude grid by weighted averaging, and a mask is used to set the values to zero in regions where the estimate is too noisy. HRET includes mode 1 and mode 2 internal tides, but mode 2 is very weak in the present study area.

**1.2- Evidence of IT propagation at different scales:**

The snapshots in Figure 2a show very fine-scale crest-like structures superimposed on positive and negative SLA spaced tens and hundreds of kilometers apart. The scenario repeats itself on the other cycles (see movie in the supplementary material), indicating that SWOT likely sees internal waves of different spatial scales. We submitted the SLA to spectral analysis to learn more about its frequency and wavelength. The 2D FFT spectra are computed in the time (cycles) and along-track (latitude) dimensions and then averaged over the cross-track (longitude) dimension. The Tukey 0.25 window is used for windowing. The wavenumber-frequency (Figure 3a) was integrated to derive the wavenumber spectrum (Figure 3b) and the frequency spectrum (Figure 3c).
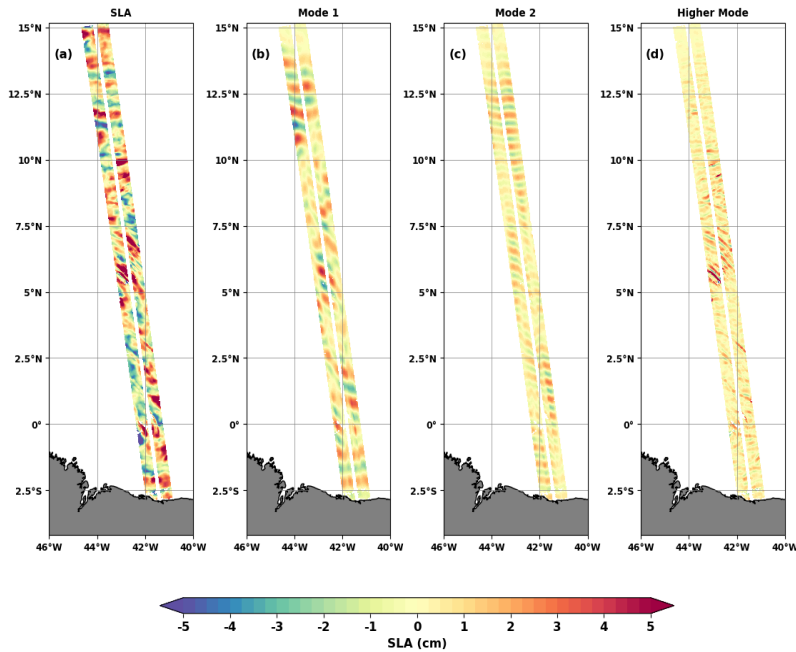
**Figure 2:** Snapshot of SWOT SLA on April 8, 2023. a) Total SLA, b) Mode 1 FFT-filtered SLA (180-90 km), c) Mode 2 FFT-filtered SLA (80-60 km) and d) Higher mode FFT-filtered SLA (50-2 km).

The wavenumber-frequency (Figure 3a), the wavenumber (Figure 3b) and the frequency (Figure 3c) spectra of SWOT SLA indicate that the dominant signal is M2 aliased to 12.22 days (see Table 1). At the M2 aliased frequency, the energy is greatest between 180-90 km and between 80-60 km (Figure 3a), leading to the spectral peaks in Figure 3b. These two wavelength bands correspond well to the theoretical baroclinic mode 1 and 2 scales expected for the internal tide in this region (Zhao, 2021). We isolated the SLA for these two wavelength bands using FFT filtering. When filtering, the FFT is calculated on the along-track dimension. Snapshots of the Mode 1 and Mode 2 SLA are shown in Figures 2b and 2c for the same day as Figure 2a, revealing more of the SLA's wave-like behavior.

Figure 2d shows the FFT-filtered SLA between 50-2km. This band contains all the small-scale structures, including the very remarkable and intense one that appears as wave crests on the SLA. On the wavenumber-frequency spectrum (Figure 3a), the energy maximum at frequency M2 extends to scales smaller than 50 km. According to Barbot et al., (2021), this could be associated to internal tide of mode 3, mode 4 and mode 5. We therefore consider the 50-2 km band as consisting of higher modes.

6
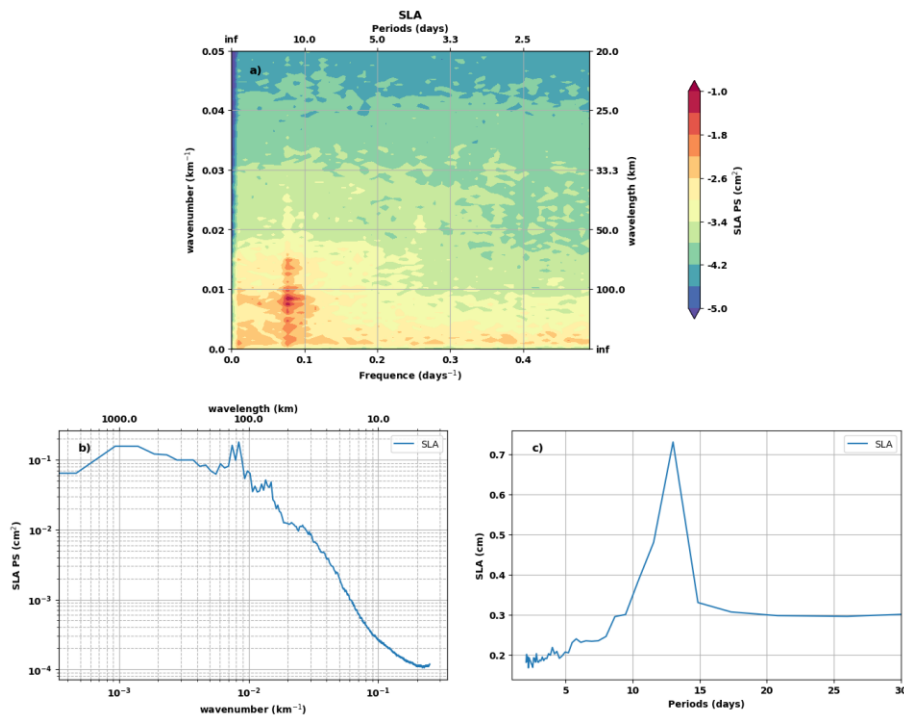
**Figure 3:** Wavenumber-frequency (a), wavenumber (c) and frequency (d) spectra of the total SLA.

**1.3- Variability analysis of IT observations:**

Analyses of SLA variability are completed by calculating the standard deviations of the total and the spatially FFT-filtered SLAs in the wavelength bands defined above.  Over the Cal/Val period, SLA varies between 1 and 5 cm under track 20 (Figure 4a). Apart from the area very close to the coastline, there are three main patches of maximum variability, each located in one of the dynamic areas highlighted in the introduction. The maximum variability of the SLA in area 1 (2.5°S-2.5°N) is mainly due to the regular mode 1 internal tide flux likely coming from sites A, B and C (Figure 4b). Mode 2 and higher modes contributions are secondary (Figures 4c and 4d) in area 1.  Higher modes have a major impact on the variability in area 2 where they make the SLA vary by 2 to 3 cm (Figure 4d), i.e. almost of the same order as mode 1 in the same area. As area 2 is far from the generation sites of the Amazonian shelf-break, the higher modes here are likely to originate from desintegration of mode 1 and mode 2. In area 3, SLA variability is driven mainly by mode 1 and mode 2.
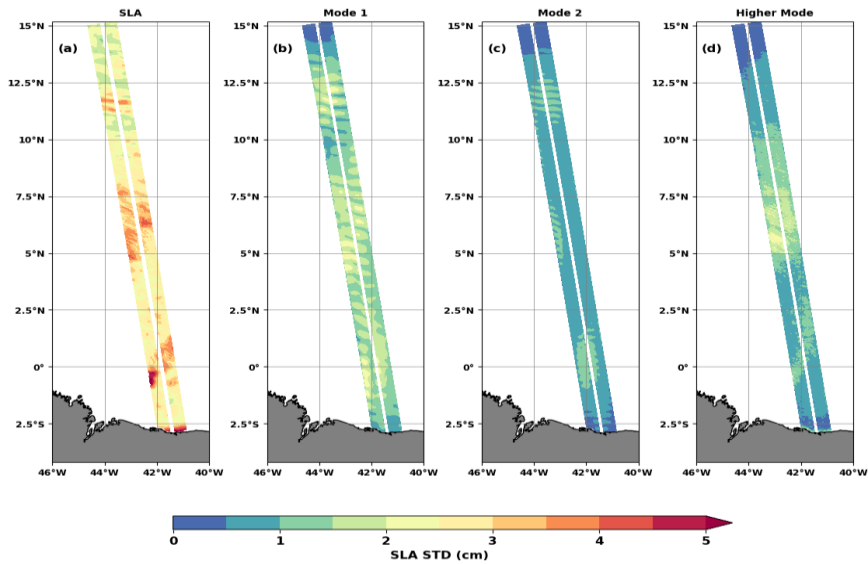
**Figure 4:** Standard deviation (in cm) of the total (a) SLA, and mode 1(b), mode 2 (c) and higher mode (d) FFT-filtered SLA.

**2- The M2, S2 and N2 coherent internal tides from SWOT: ITkars model**

In Table 1, 4 waves (M2, N2, S2, and O1) have aliasing periods shorter than the 104 days corresponding to the total length of our SWOT SLA series and are a priori of interest for our analysis. But given the Rayleigh criterion between them in Table 1, it is reasonable to restrict ourselves to the three semi-diurnal waves. Harmonic analysis based on least-squares fitting is used to extract the coherent internal tide at each band point with at least 80 valid cycles over the entire SWOT Cal/Val observation period. In the following, ITkars (IT from KARin Swot) refer to SWOT estimation of IT.
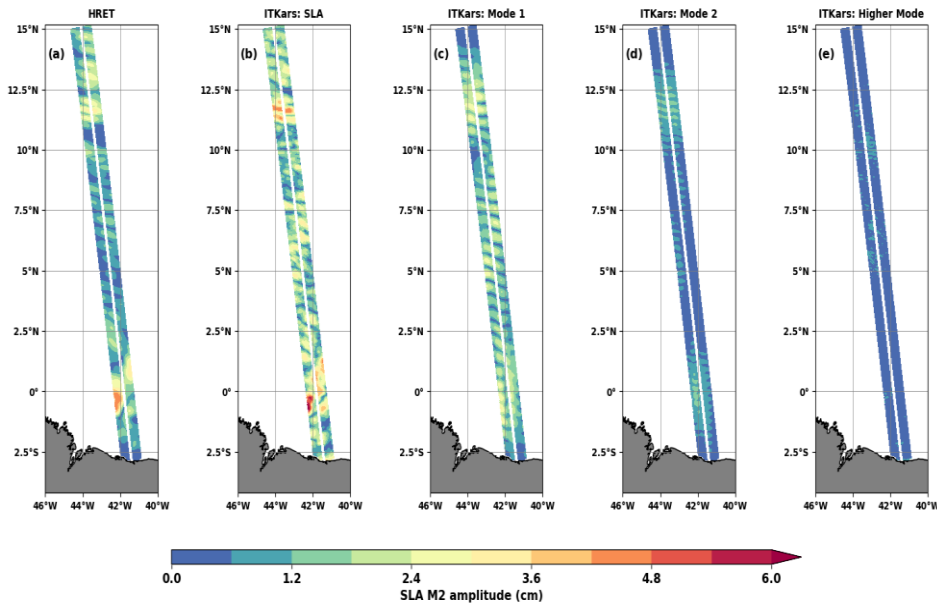
**Figure 5:** The amplitude (in cm) of the M2 internal tide from the HRET model (a) and the ITkars (b to e) model over the cal/val period. ITkars is derived by harmonic analysis of the total SWOT SLA (b) and FFT-filtered SWOT SLA for mode 1 (c), mode 2 (d) and higher mode (e) SLA. Only swath points with at least 80 valid cycles were analyzed.

The amplitudes of the coherent internal tide at the M2 frequency are presented in Figure 5 for both HRET (which include mostly mode 1 on this area) and ITkars models (which include mode 1 and mode 2). We first performed the harmonic analysis of the total SLA (Figure 5b) and repeated the harmonic analyses for each of the FFT-filtered SLAs (Figure 5c to e). The HRET model (Figure 5a) and the ITkars model based on the total SLA (Figure 5b) are similar in terms of spatial distribution, but as expected HRET has smoother and lower amplitudes because it represents a mean on many years of altimetry data. In areas 1 and 3, ITkars shows spatial features identical to those already observed on the standard deviation in Figure 4a. So, the maximum variability for these two parts of the SWOT track is indeed due to the M2 coherent internal tide. The discrepancies between standard deviations (Figure 4) and internal tide amplitudes (Figure 5) are best seen by directly comparing the maps for the different modes or wavelength bands. In area 2, the amplitude of the coherent internal tide is less than 1.5 cm for the higher modes (Figure 5e), whereas at these scales the standard deviation is maximal (Figure 4d). The high variability of the SLA found in area 2 is evidently related to internal tide incoherency.

As S2 from HRET shows unexpected patterns (not shown) and, and N2 is not available in HRET,we show only ITkars results in Figure 6. Both waves have smaller amplitudes than M2 and do not have the same structure as the latter. As the semi-diurnal S2 and N2 IT should have similar patterns to M2, those results indicate that these frequencies are certainly contaminated by other tidal waves due to poor separability on the available period (see Table 1) and are likely also contaminated by the mesoscale. Can we hope to improve our estimate of the coherent internal tide from SWOT observations?

9

243
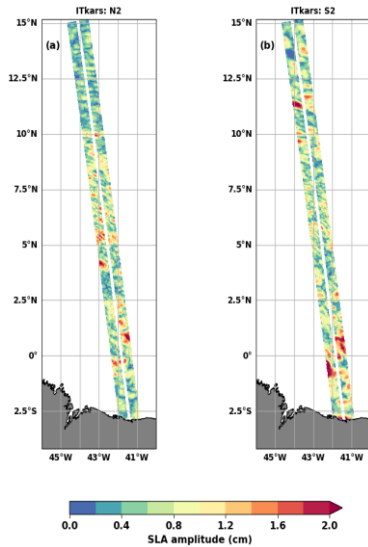
**Figure 6**: The amplitude (in cm) of the N2 (a) and S2 (b) internal tide of the ITkars model derived by harmonic analysis of the total SLA over the Cal/Val period. Only swath points with at least 80 valid cycles were analyzed.

**3- An attempt to improve the estimation of coherent internal tide from SWOT Cal/Val data: Using principal component analysis (PCA) to separate SLA content**

**3.1- Separation using PCA**

PCA, also known as EOF (Empirical Orthogonal Function), is a statistical analysis technique for reducing the dimensionality of a data set (Jolliffe, 1986). Applied to geophysical data, PCA separates the total signal into independent spatial patterns associated with independent temporal components (Principal Component) and gives a measure of the relative importance of each pattern (a percentage of the total variance). The first principal components (PC) capture most of the variance in the data and generally have a repetitive and persistent structure, thus behaving approximately like the stationary component of the signal. In particular, coherent internal tides have significant spatial correlations that PCA could identify and isolate. On this basis, we believe that PCA applied to our total SLA can help better isolate the coherent internal tide (which is stationary) from the remaining residual tidal (incoherent internal tides) and non-tidal signals observed by SWOT. Egbert and Erofeeva (2021) have successfully used PCA to determine the characteristics of the incoherent internal tide around the Amazon shelf. In this paper we focus on the coherent internal tide. Therefore, we performed the PCA on the 104 cycles of the SWOT KaRin total SLA as defined in Equation 1. At each point in the swath, we filled in the missing value with the local time mean, then normalized the ~~time series~~SLA to ensure that the ~~time~~global mean~~,~~ and ~~the~~ standard deviation become zero and one respectively. The covariance matrix is calculated on the normalized SLA, the PCA focuses on eigenvalues and not absolute values.

The two leading PCA modes shown in Figure 7 account for ~~12.3~~14.05% (PCA1, Figure 7a and c) and ~~9.1~~10.46% (PCA2, Figure 7b and d) of the total variance. Their spatial patterns correspond to IT

10

270 structures: on PCA1 (Figure 7a) the IT is intensified in area 1 and area 3, while PCA2 (Figure 7c) is
271 characterized by an increase of the IT intensity in area 2.  PCs show 12–13 days oscillations with
272 modulations around 70 days (Figure 7b and 7d), therefore recalling the aliasing periods of M2 and S2
273 waves (see table 1).  To get a more precise idea of the wavelengths and frequencies contained in PCA1
274 and PCA2, we reconstructed the SLA for both components (SLA_pca1 and SLA_pca2) and calculated
275 the spectra shown in Figure 8 (blue line for PCA1 and orange line for PCA2).



276



277

278



279
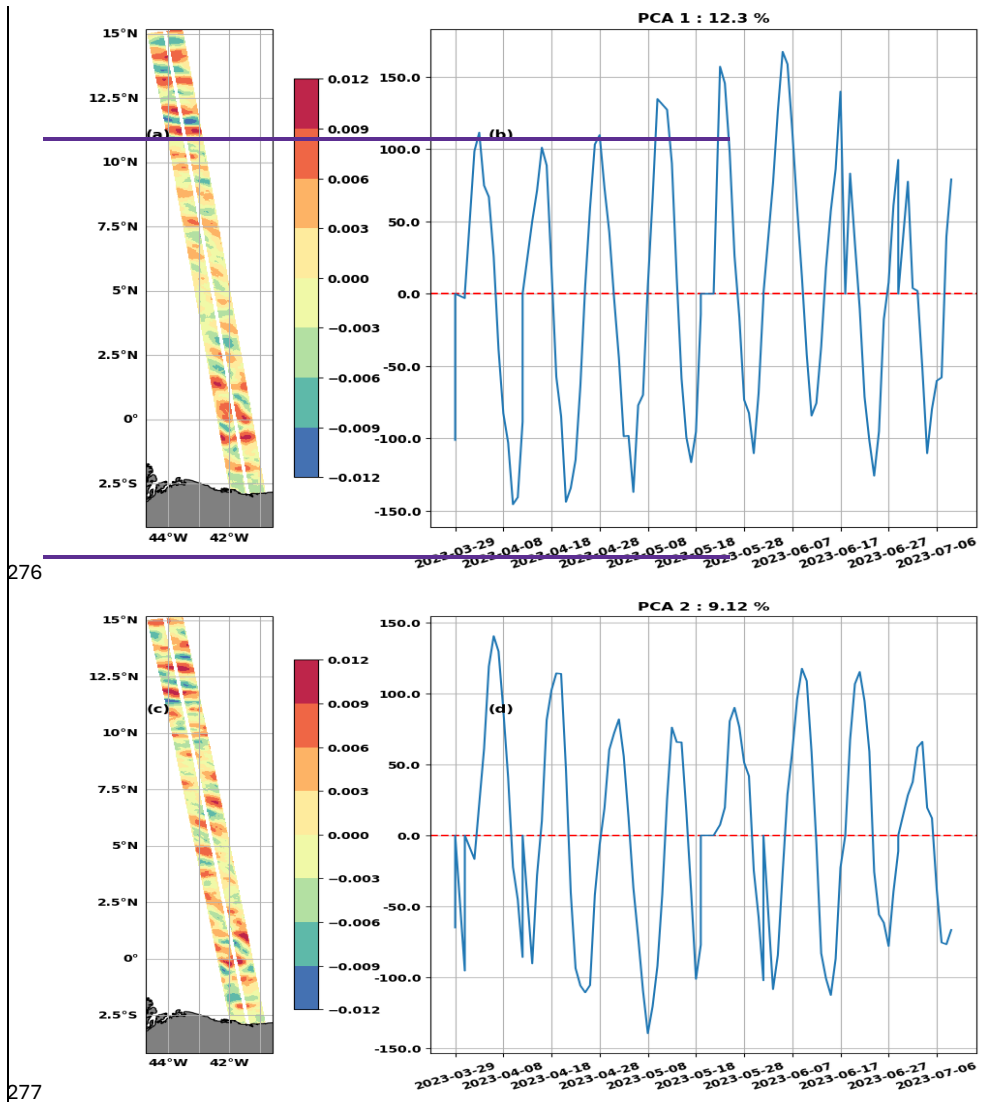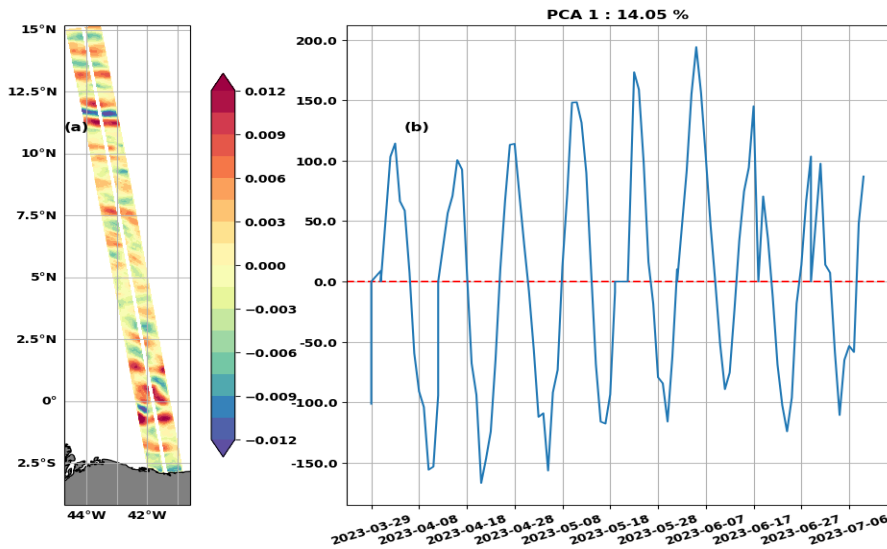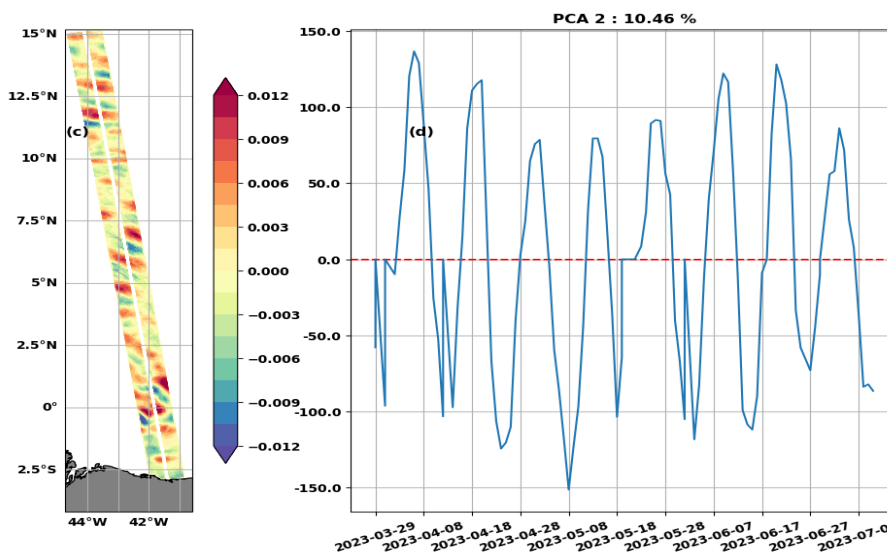
**Figure 7:** Spatial (left) and principal (right) components of PCA1 (top) and PCA2 (bottom) of the SLA along SWOT swaths over the Cal/Val period.

The wavenumber spectra (Figure 8a) indicate that PCA1 and PCA2 consist mainly of mode 1 (180-90 km) and mode 2 (80-60 km) IT.  A peak that could be associated with mode 3 stands out on the PCA2 spectrum, but overall, the energy levels of both spectra remain low for higher modes (50-2 km). The frequency spectra (Figure 8b) confirm that M2 is the dominant signal. At this frequency, the mean SLA amplitudes are 0.52 cm for PCA1 and 0.45 cm for PCA2, respectively 71% and 61% of the 0.73 cm associated with the peak of the total SLA reported by the solid black line in Figure 8b. Amplitudes are

288    low for other frequencies. The 104 available cycles are not enough to observe 70-days modulation on
289    the frequency spectra. Given the wavenumber and frequency spectra, we can say that PCA1 and PCA2
290    are two complementary representations of the propagation and evolution of the M2 dominant internal
291    tide, so they can be merged to form a single signal.  We have summed SLA_pca1 and SLA_pca2 into
292    SLA_pca_L2 (L2 refers to lower or equal to 2). A snapshot of SLA_pca_L2 is shown in Figure 9a for the
293    same cycle as in Figure 2. Interestingly, the SLA reconstructed with PCA1 and PCA2 have similar
294    patterns to the mode 1 and mode 2 FFT-filtered SLAs (Figures 2b and 2c).

295    Between PCA3 and PCA1~~2~~0 the variance explained is less than 3.~~5~~58% per PCA, from PCA1~~3~~1
296    onwards, the variance becomes less than 2% (not shown). The PCs are a mixture of several wave
297    frequencies, with M2 of lower intensity than in PCA1 and PCA2, high frequency (faster than 10 days)
298    and low frequency (15, 17 or even 25 days). It is difficult to associate the spatial patterns of these PCAs
299    with the propagation of a persistent IT in time and along the track, or even with a mode of ocean
300    variability to our knowledge. The last 3 PCA patterns resemble residual noise from the processing of
301    raw SWOT data. We grouped PCA3 to PCA104 into SLA_pca_G2 (G2 for greater than 2).   The small-
302    scale structures that were identified in Figure 2a are clearly visible in the snapshot of the SLA_pca_G2
303    in Figure 9b. Figures 9a and 9b are complementary, as the PCA acted as a filter. The total SLA is now
304    split into SLA_pca_L2 and SLA_pca_G2. The spectra of SLA_pca_G2 are shown in green in Figure 8.
305    Nearly all energies for scales above 180 km (seen as large scale) and below 50 km (for higher modes)
306    are found in the wave number spectrum of SLA_pca_G2. Around the aliased frequency of M2, the
307    mean amplitude is 0.19 cm for SLA_pca_G2. This is about a quarter of the mean amplitude of the total
308    SLA (0.73 cm). With such a drop in the energy of the spectrum, it's tempting to say that separation by
309    the PCA has acted in the same way as a classical detiding. To verify this, we calculated the spectra of
310    the total SLA detided with M2 from ITkars and plotted them as a dashed black line in Figure 8. At all
311    frequencies and wavelengths, they overlap well with the spectra of SLA_pca_G2. Therefore,
312    SLA_pca_G2 is more representative of the incoherent internal tide and SLA_pca_L2 is more suitable
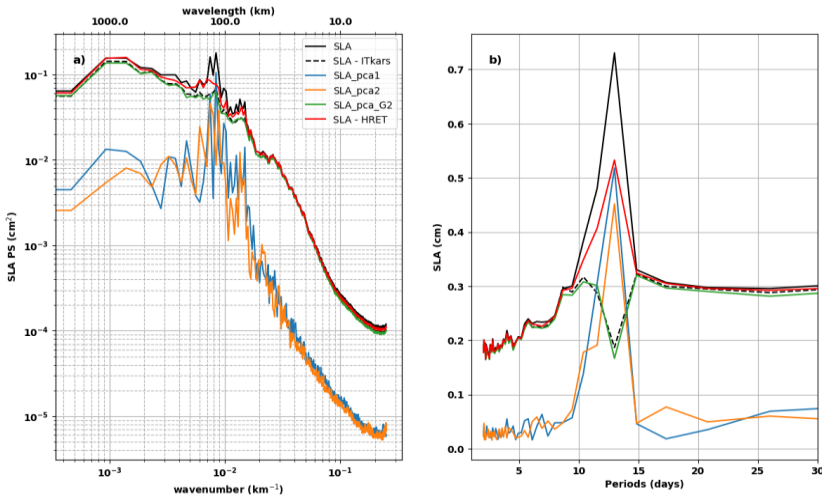313    for improving the estimation of the coherent internal tide.

317



318
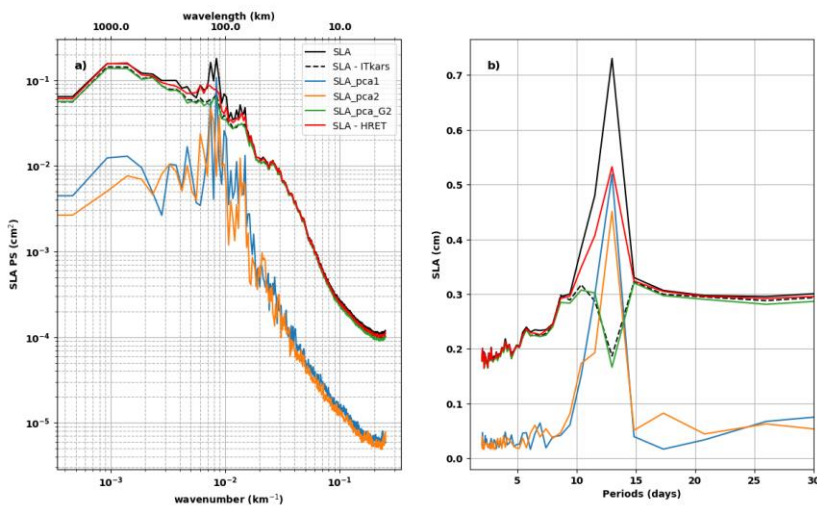
**Figure 8:** Wavenumber (a) and frequency (b) spectra of SLA_pca1 ( in blue), SLA_pca2 (in orange), SLA_pca_G2 (in green), SLA – HRET (in red) and SLA - ITkars (black dashed line). SLA_pca_G2 is the sum of the SLAs of PCAs greater than 2. The spectra of total SLA (black solid line) from Figure 3 are reported here. ITKars is the internal tide model derived from SWOT KaRIn data (cf in section 2).



323

14
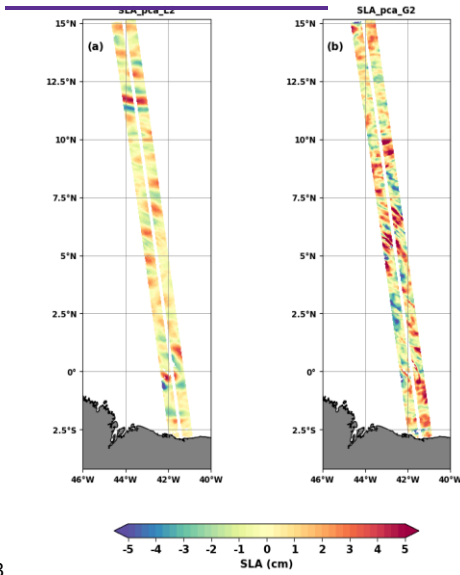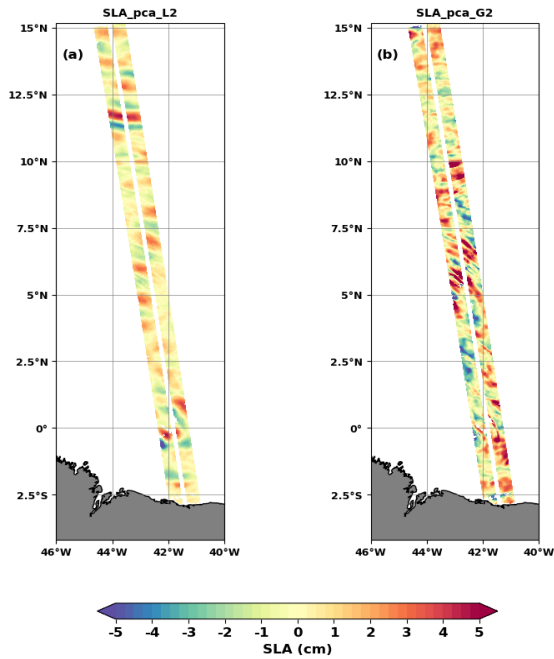
**Figure 9:** Snapshot of SWOT SLA_pca_L2 (a) and SLA_pca_G2 (b) on 08 April, 2023 (as in Figure 2). SLA_pca_L2 is the sum of the SLAs of PCs less than or equal to 2 (PC1 and PC2).
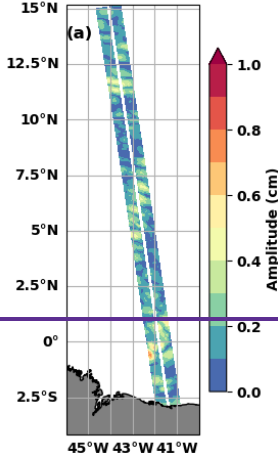
### 3.2- ITkars_pca internal tide model

We have performed the harmonic analysis of SLA_pca_L2 at the semi-diurnal frequencies M2, N2 and S2 (Figure 10). The resulting internal tide amplitude (model) is referred to as ITkars_pca to distinguish it from ITkars based solely on harmonic analysis of SWOT Karin data. Compared to Figure 6 corresponding to ITkars, the ITkars_pca internal tide maps for N2 (Figure 10a) and S2 (Figure 10b) are cleared of small scales, and the patterns for both waves are now close to that of M2 as expected (Figure 10c and 5b reported in 10f). At first glance, there seems to be no difference between ITkars (Figure 5b or 10f) and ITkars_pca (Figure 10c) for M2. By making the complex difference between the two signals (Figure 10c and 10f), we deduce the amplitude shown in Figure 10d, which is equivalent to the amplitude of the harmonic analysis of SLA_pca_G2 at M2. As with N2 and S2, Figure 10d shows that M2 ITkars (Figure 5b or 10f) also contains an additional signal dominated by small scales, and which does not resemble the classic internal tide.
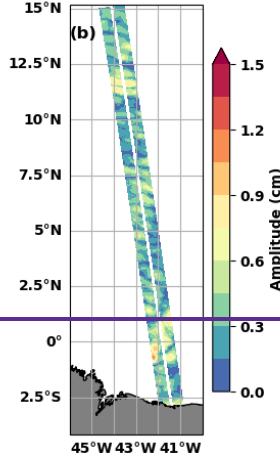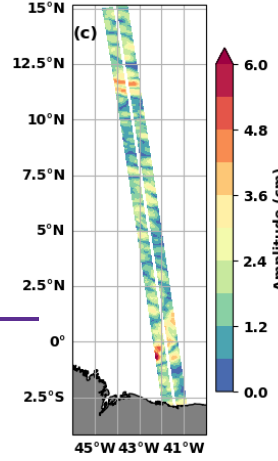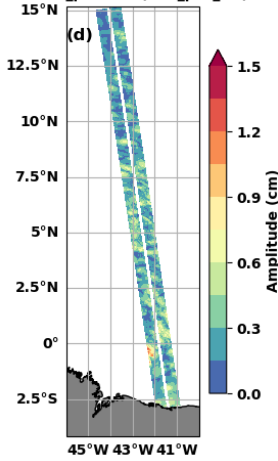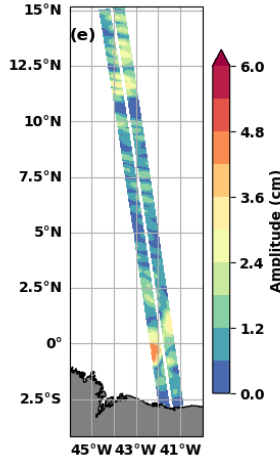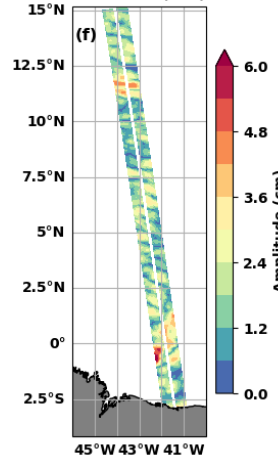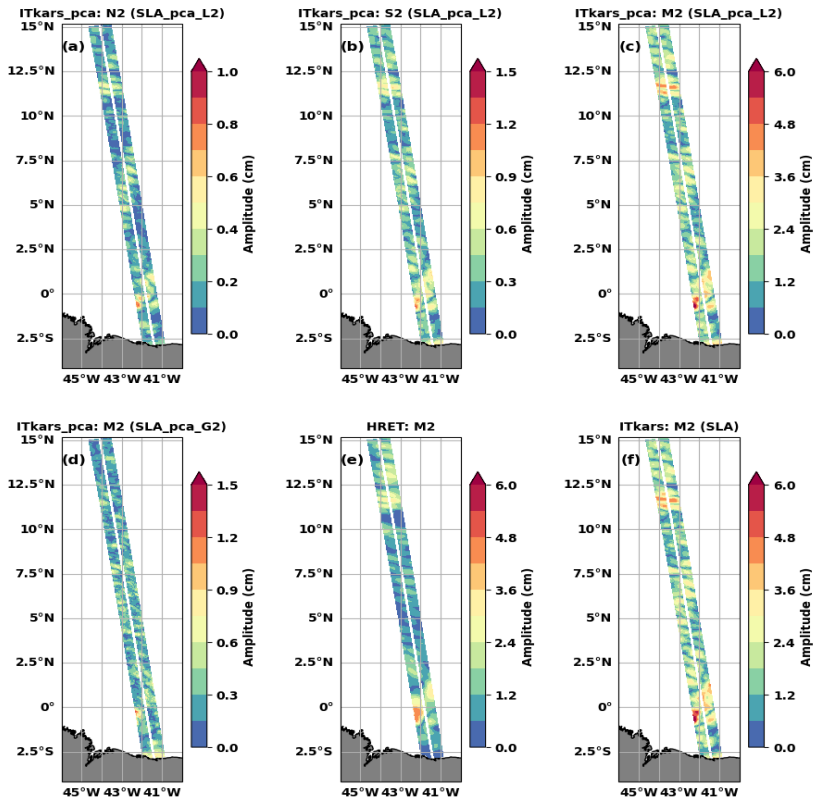
**Figure 10**: The amplitude (in cm) of the internal tides N2 (a), S2 (b) and M2 (c and d) of the ITkars_pca model derived by harmonic analysis of SLA_pca_L2 (a to c) and SLA_pca_G2 (d) over the Cal/Val period. SLA_pca_L2 is the SLA based on PCA1 and PCA2, SLA_pca_G2 is compiled from PCA3 to PCA104. Only swath points with at least 80 valid cycles were analyzed. Figure 5a and 5b are reported here, M2 HRET (e) and M2 ITkars (f).

The origin of the extra signal contaminating ITkars could be dynamic or numerical. Dynamically, these could be very intense non-linear waves, solitons, or incoherent internal tides, which are retained in the harmonic analysis of section 2 due to the short length of the time series. On the numerical side, noise linked to the pre-processing of SWOT data cannot be ruled out. Another source of contamination could also be the DUACS correction we apply beforehand to distinguish internal tides.

## 4 - Complementary comparison between SWOT and HRET IT models: predictability of internal tides

The comparison between HRET and SWOT based internal tides models (ITkars and ITkars_pca) is taken a step further in this final section. Each of the atlases (amplitude and phase) will be used as an internal tide correction model for the SWOT data. This involves making internal tide predictions over a given period and then subtracting these predictions from raw observations. Various metrics are used to quantify the capability of each model to reduce the variance.

In Figure 8, the ITkars M2 atlas has been used as a correction model to detide the total SLA over the entire Cal/Val observation period (black dashed line). We have done the same with M2 from HRET and the corresponding spectra is shown in red in Figure 8. As in figure 3, the 1D spectra are integrations of the 2D wavenumber-frequency spectrum. On the wavenumber spectra, the peaks of modes 1 and 2 are reduced but remain visible whatever the detiding applied (Figure 8a). We have integrated the wavenumber spectra of the total SLA (Black line in Figure 8) and the detided SLA (Black dashed and red line in Figure 8) over all wavelengths, between 180 and 90 km for mode 1, between 80 and 60 km for mode 2, from 50 to 2 km for the higher modes, and finally over wavelengths greater than 180 km for the large scale. The derived standard deviations are presented in Table 2 for the total SLA and the SLA detided with ITkars or HRET, as well as the percentages expressing the residual variance rate (ratio of the variances of the detided SLA on the total SLA). The higher is the standard deviation of the detided SLA or the percentage in Table 2, the less efficient is the correction used for detiding. According to Table 2, the application of the M2 internal tide prediction of each of the models removes very little variance from the SLA, nevertheless ITkars is more efficient than HRET especially at mode 1 and mode 2 scales. For these scales, the residual variance reaches 76% and 84% of the SLA after correction by ITkars and is likely to be incoherent internal tide. For the higher modes, Table 2 agrees with Figure 5e: the M2 correction has no effect on these scales. ITkars has a greater impact on large scale SLAs than HRET: HRET has almost no signal at large scale by construction, while ITkars can capture some variability at large scales due to short time-series and no fitting approximation. When detiding with ITkars, the energy spectrum (Figure 8b) decreases strongly around the aliased frequency of M2 (around 13 days, see Table 1). The mean of SLA amplitude along the SWOT swaths drops by 74% (from 0.73 cm to 0.19 cm) after ITkars detiding at M2 frequency. With the HRET correction (Figure 8), the peak amplitude at the M2 frequency is 0.53 cm, i.e. a 27% reduction of the peak of the total SLA, which is more than twice lower than with the ITkars correction. It can also be seen that periods of more than 15 days and less than 5 days are not affected by the correction, since we have limited ourselves to M2 frequency.

**Table 2:** Comparative table of the standard deviations of total SLA and SLA detided with HRET or ITkars. Standard deviations are obtained by integrating the spectra of Figure 3c on different wavelength bands (in cm). The ratio between detided SLA and total SLA, computed as a percentage, is given in parentheses.

|  | All wavelengths | Large scales >180km | Mode 1 180 - 90km | Mode 2 80 - 60km | Higher modes 50 - 2km |
|---|---|---|---|---|---|
| Total SLA | 1.82 | 1.07 | 1.03 | 0.58 | 0.74 |
| Detided ITkars | 1.6 (88%) | 0.99 (93%) | 0.78 (76%) | 0.49 (84%) | 0.71 (96%) |
| Detided Hret | 1.71 (94%) | 1.04 (97%) | 0.89 (86%) | 0.54 (93%) | 0.73 (99%) |

The better performance of ITkars correction in comparison to HRET is not surprising, since ITkars is derived from the same database to which the detiding is applied. The result is almost identical to ITkars when the SLA is detided with M2 from ITkars_pca. This is not surprising as the amplitude of the M2 residual in SLA_pca_G2 is small (Figure 10d). To obtain the best possible comparison between ITkars and ITkars_pca still focusing on M2 wave, we propose to apply the detiding to data that are independent of those used to derive the internal tide atlas. Thus, the SWOT data were divided into two periods: period 1, comprising the first 70 cycles (from late March to early June), and period 2 (from early June to early July), comprising the last 34 cycles. We repeated the M2 harmonic analysis of the total SLA over period 1 and derived the atlas "ITkars_p1" (p1 indicates period 1). We did the same with

SLA_pca_L2 and derived the atlas "ITkars_pca_p1". The atlases ITkars_p1, ITkars_pca_p1 and HRET are then used to detide the SLA and SLA_pca_L2, first in period 1 and secondly in period 2, which is independent of period 1. Since period 2 is short for frequency spectral analysis, we're going to look at the standard deviation (Table 3) and the variance reduction (Figure 11). Variance reduction is calculated from equation 2 as the difference between the variance of corrected SLA and the variance of the uncorrected SLA (or SLA_pca_L2). A negative variance reduction indicates that the internal tide correction reduces the SLA variance.

$$\text{Variance reduction} = \text{var (SLA} - \text{M2 atlas)} - \text{var (SLA)} \qquad (2)$$

The spatial mean of the standard deviation is summarized in Table 3. On period 1, the standard deviation of the total SLA is 2.56 cm. After correction with M2 of the HRET model, the standard deviation drops by 7% (to 2.39 cm). The SLA standard deviation decreases by about 15% and 14% with ITkars_p1 and ITkars_pca_p1, respectively. The difference between the two ITkars models is not significant as we detide the same data that are used to derive the models (ITkarsp1 in particular). The application of the corrections to SLA_pca_L2 reduces the residual standard deviation from 1.33 cm to 0.99 cm for HRET, to 0.53 cm for ITkars_p1 and to 0.42 cm for ITkars_pca_p1. This shows that even in an SLA dominated by coherent internal tides, HRET removes only 15% of the variance, whereas SWOT-based internal tide models remove over 60%. ITkars_pca_p1 is obviously the best correction for SLA_pca_L2, with ITkars_p1 being slightly less efficient.

On period 2, the corrections of the SLA with the three internal tide models are less efficient. Table 3 shows that, on average, between 5% and 9% of the SLA variance is suppressed, with ITkars_pca_p1 being the best corrective internal tide model. As can be seen from the variance reduction maps (Figure 11a to c), the three models reduce variance (blue color) in the parts of the swath where the coherent internal tide signal is strong enough (Figure 10). Outside these areas, the internal tide models tend to add variance, and the variance reductions become positive. This undesirable effect of the correction models is mainly observed in the central part of the swath (area 2), where the higher modes contribute significantly to the SLA variability (see Figure 4). The effect in area 2 is pronounced for ITkars_p1 (Figure 11b), indicating a prediction failure. When considering the independent SLA_pca_L2 data (period 2, Table 3), HRET removes 21% of the variance. For ITkars_p1 and ITkars_pca_p1, the variance is reduced by 45% and 55% respectively. The impact of PCA on the derivation of the M2 internal tide atlas is highlighted here by the 10% gap between the percentages of variance reduction when applying the two models based on SWOT observations. The variance reduction figures confirm that the correction works better on SLA_pca_L2 (Figure 11 d to e). Although there are still swath locations with positive variance reduction, this is no longer concentrated in the central part. Variance reductions are dominated by negative values for ITkars_p1 (Figure 11e) and ITkars_pca_p1 (Figure 11f).

**Table3:** Comparative table of standard deviations (cm) of SLA and SLA_pca_L2 detided with either M2 HRET, M2 ITkars or M2 ITkars_pca models over period 1 (from late March to early June 2023, the first 70 cycles) and period 2 (from early June to early July 2023, the last 34 cycles). ITkars_p1 and ITkar_pca_p1 models were built on period 1 and validated on period 2. The ratio between detided SLA and total SLA is indicated in the parentheses (in percent).

|  | Period 1 | | Period 2 | |
|---|---|---|---|---|
|  | SLA | SLA_pca_L2 | SLA | SLA_pca_L2 |
| no IT correction | 2.56 | 1.33 | 2.79 | 1.15 |
| HRET | 2.39 (93%) | 0.99 (74%) | 2.64 (95%) | 0.91 (79%) |

| ITkars_p1 | 2.18 (85%) | 0.53 (40%) | 2.65 (95%) | 0.63 (55%) |
| ITkars_pca_p1 | 2.21 (86%) | 0.42 (32%) | 2.55 (91%) | 0.52 (45%) |

440

441
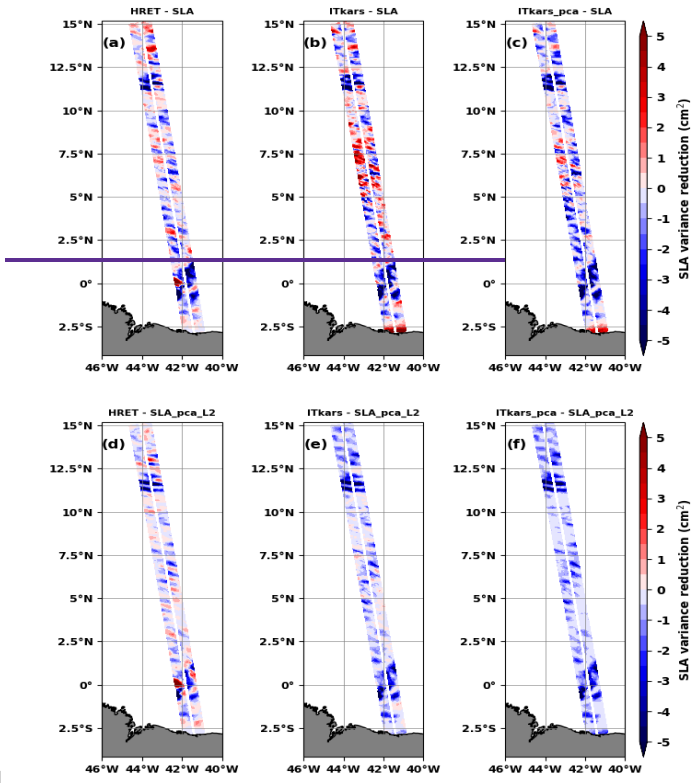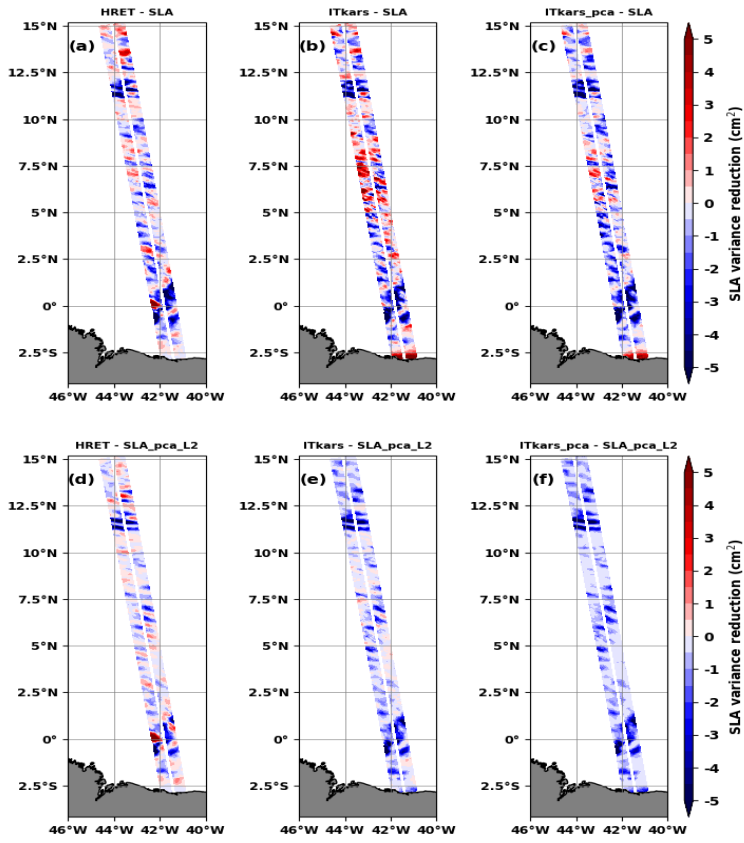
**Figure 11:** Variance reduction (in cm²) on period 2 from early June to early July (last 34 cycles) when using either M2 HRET (left column) or M2 ITkars_p1 (middle column) or M2 ITkars_pca_p1 (right column) to correct the total SLA (top line) or SLA_pca_L2 (bottom line).

## 4- Discussion and perspectives

In this study, we explored and characterized the internal tide signal in SWOT KaRIn observations over the Cal/Val period (1-day orbit) between late March and early July 2023 (104 cycles) and along the track 20 located off the Amazon shelf in the tropical Atlantic between 2°S and 15°N. The internal tide as seen by SWOT is a mixture of several spatial scales, including baroclinic modes 1 and 2 defined by wavelengths between 180-90 km and 80-60 km respectively. SWOT also sees very intense fine-scale structures (wavelengths between 50-2 km) that we have associated with higher baroclinic modes, including modes 3, 4 and 5 according to Barbot et al., (2021). As a result, SWOT seems to live up to expectations, providing a direct 2D view of the internal tide sea surface signatures and even access to smaller scales.

458    Our approach to extract the internal tide signal through the 1-day SWOT data consisted firstly of
459    filtering the large scale (including the mesoscale) by subtracting the DUACS MSLA from the SWOT
460    observations; then we reintroduced the internal tide correction HRET from Zaron (2019) to obtain a
461    SLA consisting of the total internal tide signal. We either performed the harmonic analysis (as in section
462    2) or proceeded upstream to the PCA before the harmonic analysis (as in section 3). The internal tide
463    model based on harmonic analysis of SWOT KaRin data was referenced ITkars (Internal Tide from KaRin
464    Swot), the one obtained by combining PCA and harmonic analysis ITkars_pca. We focused on the semi-
465    diurnal frequencies M2, S2 and N2.

466    Spatial patterns of M2 internal tides from ITkars and ITkars_pca models agreed with the M2 HRET
467    model based on nearly 25 years of conventional altimeter (nadir) observations. The similarities
468    between models based on SWOT Karin and model with conventional altimeter are partly linked to the
469    fact that SWOT data are analyzed over March to July during which the internal tide is most stable and
470    coherent off the Amazon shelf (Tchilibou et al., 2022). One consequence of analyzing SWOT data over
471    this short 104-day window is that the amplitude of the internal tide is stronger with SWOT estimation
472    than with HRET. This result is logical since the intensity of the coherent internal tide depends on the
473    length of the time series analyzed: a longer time series allows a better estimate of the coherent signal
474    which is therefore smoother (Ansong et al.,2015; Zhou et al.,2015; Nash et al.,2012). The separation
475    of M2 from O1 is not ensured with 104 cycles of SWOT 1-day data, however, in this region the
476    amplitude of the internal tide is negligible at O1 frequency compared to M2 (see Figure 1 in Tchilibou
477    et al.,2022), so M2 ITkars_pca is thus quite reliable.

478    The maps of N2 and S2 highlight the contamination of ITkars by signals other than the coherent
479    internal tide, and particularly by very small scales. We hypothesize that the contamination is due to
480    the leakage of nonlinear waves, incoherent internal tides, and ocean variability in the harmonic
481    analyses. Regarding ocean variability, part of it is not captured by DUACS and was therefore not
482    subtracted from the SLA. Moreover, subtracting the mesoscale, as we have done, is itself a possible
483    source of error in estimating the internal tide (Zaron and Ray, 2018). One way to reduce the effects of
484    contamination by ocean circulation would be to apply a simultaneous internal tide and mesoscale
485    inversion method as proposed by Ubelmann et al. (2022). The combination of PCA and harmonic
486    analysis gives semi-diurnal ITkars_pca maps (M2, S2 and N2) with similar patterns. The amplitude of
487    N2 ITkars_pca deduced from SWOT is of the same order as that in the new product HRET14 (Zaron and
488    Elipot 2024). The result is encouraging for S2, especially as the length of the 1-day observations is not
489    sufficient to correctly separate it from waves such as Sa and Ssa, whose periods are identical to those
490    of the annual and semi-annual variation of the ocean. A longer time series is needed to better separate
491    the internal tide components from SWOT observation, and we will consider analyses of the 21-day
492    SWOT science orbit data when the time series will be long enough.

493    PCA has improved our estimate of the internal tide model from the SWOT KaRin data. From the
494    PCA we kept the first two main modes (PCA1 and PCA2) and considered them as the coherent internal
495    tide given their fairly stationary character. Thus, the coherent internal tide accounts for ~~21.42%~~
496    ~~(12.3~~24.51% (14.05 of PCA1 and ~~9.12~~10.46 of PCA2) of SLA variance in 1-day SWOT observations, a
497    proportion in line with the studies of Zaron (2017) and Egbert and Erofeeva (2021) in this region. The
498    coherent internal tide isolated through the PCA consists of mode1, mode 2 noticeable in PCA1 and
499    PCA2. The fact that the coherent internal tide signal is projected onto two main modes of the PCA is
500    an open question. The principal components of PCA1 and PCA2 are shifted by 3 to 4 days, about a
501    quarter of the aliased frequency of M2, which could correspond to a phase quadrature, as there is
502    between the imaginary and real parts needed to reconstruct a sinusoidal signal. Instead of being the
503    real and imaginary parts of a signal, PCA1 and PCA2 could also represent the same phenomenon and

504 highlight its evolution in area 2 in the middle of the swaths: the moderation of internal tides in area 2
505 with PCA1 and their intensification with PCA2. This type of PCA/EOF behavior is observed in the case
506 of ENSO studies in the Pacific (Takahashi et al., 2011). The peaks on the wave number spectrum of
507 PCA1 and PCA2 are shifted by few kilometers at the mode 1 and mode 2 scales, suggesting a change in
508 wavelengths relating to changes in stratification conditions as suggested by Barbot et al. (2021). A
509 longer series of Cal/Val observations could have helped to better distinguish PCA1 from PCA2.

510 The principal components (time series) of PCA1 and PCA2 provide an overview and an opportunity
511 to study the daily variability of internal tide amplitude, a perspective difficult to access with
512 conventional altimetry missions. This opportunity to learn more about the temporal variability of the
513 internal tide using a single high-resolution mission is lost, or at least postponed, with SWOT's switch
514 to its 21-days scientific orbit. One of the limitations of using PCA to analyze SWOT data is probably its
515 sensitivity to track length. The total variance is distributed differently in the principal components
516 depending on whether the track is long or short, or whether ocean dynamics change significantly along
517 the track. It would be interesting to look at this point in the perspective of a global model, for example.
518 We are curious to know how the PCA will behave in the case of multi-track use, and at their crossing
519 points.

520 In the context of 1-day SWOT observations, the use of PCA can be useful in determining wave
521 frequencies of interest for the development of the coherent internal tide model. The combination of
522 PCA and harmonic analysis further reveals the observational potential of SWOT. We are currently
523 working on other SWOT tracks in various ocean regions to test the robustness of our method
524 combining PCA and harmonic analysis. We also plan to explore in situ observations of the SWOT Cal/Val
525 and other databases to understand better our results. Work remains to be done to confirm the
526 presence of mode 3 in the coherent internal tide signal in this region. The incoherence of the internal
527 tide and its interaction with the circulation are other issues to be addressed with these SWOT data.

528 The final issue addressed in this study was the correction of the internal tide signal in the SWOT 1-
529 day observations. On average, the HRET model corrects only 6% of the SLA variance over the Cal/Val
530 period, while ITkars based on SWOT observations corrects 12% (Table 2). These percentages are low
531 due to the high degree of internal tides incoherency in this part of the ocean. However, they indicate
532 that the HRET correction is not efficient enough. It would be more relevant to directly evaluate the
533 internal tide signals on 1-day SWOT observations and then use it as a correction model. The harmonic
534 analysis may be sufficient if the aim is to apply the tidal model to the same data, but if not, the previous
535 step of the PCA is recommended to obtain a more realistic model. The question of correcting internal
536 tides and improving internal tide models will also remain a challenge for the exploitation of SWOT's
537 21-day cycles.

538

544
545 **References:**

546 Aguedjou, H. M. A., Dadou, I., Chaigneau, A., Morel, Y., and Alory, G.: Eddies in the Tropical Atlantic
547 Ocean and Their Seasonal Variability, Geophysical Research Letters, 46, 12156–12164,

548    https://doi.org/10.1029/2019GL083925, 2019.

549    Alford, M. H., Peacock, T., MacKinnon, J. A., Nash, J. D., Buijsman, M. C., Centurioni, L. R., Chao, S.-Y.,
550    Chang, M.-H., Farmer, D. M., Fringer, O. B., Fu, K.-H., Gallacher, P. C., Graber, H. C., Helfrich, K. R.,
551    Jachec, S. M., Jackson, C. R., Klymak, J. M., Ko, D. S., Jan, S., Johnston, T. M. S., Legg, S., Lee, I.-H., Lien,
552    R.-C., Mercier, M. J., Moum, J. N., Musgrave, R., Park, J.-H., Pickering, A. I., Pinkel, R., Rainville, L., Ramp,
553    S. R., Rudnick, D. L., Sarkar, S., Scotti, A., Simmons, H. L., St Laurent, L. C., Venayagamoorthy, S. K.,
554    Wang, Y.-H., Wang, J., Yang, Y. J., Paluszkiewicz, T., and (David) Tang, T.-Y.: The formation and fate of
555    internal waves in the South China Sea, Nature, 521, 65–69, https://doi.org/10.1038/nature14399,
556    2015.

557    Ansong, J. K., Arbic, B. K., Buijsman, M. C., Richman, J. G., Shriver, J. F., and Wallcraft, A. J.: Indirect
558    evidence for substantial damping of low-mode internal tides in the open ocean, JGR Oceans, 120,
559    6057–6071, https://doi.org/10.1002/2015JC010998, 2015.

560    Arbic, B., Richman, J., Shriver, J., Timko, P., Metzger, J., and Wallcraft, A.: Global Modeling of Internal
561    Tides    Within    an    Eddying    Ocean    General    Circulation    Model,    oceanog,    25,    20–29,
562    https://doi.org/10.5670/oceanog.2012.38, 2012.

563    Assene, F., Koch-Larrouy, A., Dadou, I., Tchilibou, M., Morvan, G., Chanut, J., Costa Da Silva, A.,
564    Vantrepotte, V., Allain, D., and Tran, T.-K.: Internal tides off the Amazon shelf – Part 1: The importance
565    of the structuring of ocean temperature during two contrasted seasons, Ocean Sci., 20, 43–67,
566    https://doi.org/10.5194/os-20-43-2024, 2024.

567    Bai, X., Lamb, K. G., and Da Silva, J. C. B.: Small-Scale Topographic Effects on the Generation of Along-
568    Shelf Propagating Internal Solitary Waves on the Amazon Shelf, JGR Oceans, 126, e2021JC017252,
569    https://doi.org/10.1029/2021JC017252, 2021.

570    Ballarotta, M., Ubelmann, C., Veillard, P., Prandi, P., Etienne, H., Mulet, S., Faugère, Y., Dibarboure, G.,
571    Morrow, R., and Picot, N.: Improved global sea surface height and current maps from remote sensing
572    and in situ observations, Earth Syst. Sci. Data, 15, 295–315, https://doi.org/10.5194/essd-15-295-2023,
573    2023.

574    Ballarotta, M., Ubelmann, C., Pujol, M.-I., Taburet, G., Fournier, F., Legeais, J.-F., Faugère, Y.,
575    Delepoulle, A., Chelton, D., Dibarboure, G., and Picot, N.: On the resolutions of ocean altimetry maps,
576    Ocean Sci., 15, 1091–1109, https://doi.org/10.5194/os-15-1091-2019, 2019.

577    Barbot, S., Lyard, F., Tchilibou, M., and Carrere, L.: Background stratification impacts on internal tide
578    generation and abyssal propagation in the western equatorial Atlantic and the Bay of Biscay, Ocean
579    Sci., 17, 1563–1583, https://doi.org/10.5194/os-17-1563-2021, 2021.

580    Brandt, P., Rubino, A., and Fischer, J.: Large-Amplitude Internal Solitary Waves in the North Equatorial
581    Countercurrent,    J.    Phys.    Oceanogr.,    32,    1567–1573,    https://doi.org/10.1175/1520-
582    0485(2002)032<1567:LAISWI>2.0.CO;2, 2002.

583    Buijsman, M. C., Arbic, B. K., Richman, J. G., Shriver, J. F., Wallcraft, A. J., and Zamudio, L.: Semidiurnal
584    internal    tide    incoherence    in    the    equatorial    Pacific,    JGR    Oceans,    122,    5286–5305,
585    https://doi.org/10.1002/2016JC012590, 2017.

586    Carrere, L., Arbic, B. K., Dushaw, B., Egbert, G., Erofeeva, S., Lyard, F., Ray, R. D., Ubelmann, C., Zaron,
587    E., Zhao, Z., Shriver, J. F., Buijsman, M. C., and Picot, N.: Accuracy assessment of global internal-tide
588    models using satellite altimetry, Ocean Sci., 17, 147–180, https://doi.org/10.5194/os-17-147-2021,
589    2021.

590  Chelton, D. B., Schlax, M. G., and Samelson, R. M.: Global observations of nonlinear mesoscale eddies,
591  Progress in Oceanography, 91, 167–216, https://doi.org/10.1016/j.pocean.2011.01.002, 2011.

592  De Macedo, C. R., Koch-Larrouy, A., Da Silva, J. C. B., Magalhães, J. M., Lentini, C. A. D., Tran, T. K., Rosa,
593  M. C. B., and Vantrepotte, V.: Spatial and temporal variability in mode-1 and mode-2 internal solitary
594  waves from MODIS-Terra sun glint off the Amazon shelf, Ocean Sci., 19, 1357–1374,
595  https://doi.org/10.5194/os-19-1357-2023, 2023.

596  Dibarboure, G., Anadon, C., Briol, F., Cadier, E., Chevrier, R., Delepoulle, A., Faugère, Y., Laloue, A.,
597  Morrow, R., Picot, N., Prandi, P., Pujol, M.-I., Raynal, M., Treboutte, A., and Ubelmann, C.: Blending 2D
598  topography images from SWOT into the altimeter constellation with the Level-3 multi-mission DUACS
599  system, EGUsphere [preprint], https://doi.org/10.5194/egusphere-2024-1501, 2024.

600  Duda, T. F., Lin, Y.-T., Buijsman, M., and Newhall, A. E.: Internal Tidal Modal Ray Refraction and Energy
601  Ducting in Baroclinic Gulf Stream Currents, Journal of Physical Oceanography, 48, 1969–1993,
602  https://doi.org/10.1175/JPO-D-18-0031.1, 2018.

603  Dufau, C., Orsztynowicz, M., Dibarboure, G., Morrow, R., and Le Traon, P.: Mesoscale resolution
604  capability of altimetry: Present and future, JGR Oceans, 121, 4910–4927,
605  https://doi.org/10.1002/2015JC010904, 2016.

606  Dunphy, M. and Lamb, K. G.: Focusing and vertical mode scattering of the first mode internal tide by
607  mesoscale eddy interaction, JGR Oceans, 119, 523–536, https://doi.org/10.1002/2013JC009293, 2014.

608  Dunphy, M., Ponte, A. L., Klein, P., and Le Gentil, S.: Low-Mode Internal Tide Propagation in a Turbulent
609  Eddy Field, Journal of Physical Oceanography, 47, 649–665, https://doi.org/10.1175/JPO-D-16-0099.1,
610  2017.

611  Dushaw,B. D:  An Empirical Model for Mode-1 Internal Tides Derived from Satellite Altimetry:
612  Computing Accurate Tidal Predictions at Arbitrary Points over the World oceans, Technical
613  Memorandum APL-UW TM: https://apl.uw.edu/project/project.php?id=tm_1-15, (last access: 2 June
614  2024), 2015.

615  Egbert, G. D. and Erofeeva, S. Y.: An Approach to Empirical Mapping of Incoherent Internal Tides With
616  Altimetry Data, Geophysical Research Letters, 48, e2021GL095863,
617  https://doi.org/10.1029/2021GL095863, 2021.

618  Fu, L.-L. and Ubelmann, C.: On the Transition from Profile Altimeter to Swath Altimeter for Observing
619  Global Ocean Surface Topography, Journal of Atmospheric and Oceanic Technology, 31, 560–568,
620  https://doi.org/10.1175/JTECH-D-13-00109.1, 2014.

621  Fu, L.-L., Alsdorf, D., Rodriguez, E., Morrow, R., Mognard, N., Lambin, J., Vaze, P., and Lafon, T.: THE
622  SURFACE WATER AND OCEAN TOPOGRAPHY (SWOT) MISSION, California, CA: JPL publication, 2012.

623  Gill, A. E.: Atmosphere-ocean dynamics, Nachdr., Acad. Press, San Diego, 662 pp., 2006.

624  Jackson, C., Da Silva, J., and Jeans, G.: The Generation of Nonlinear Internal Waves, oceanog, 25, 108–
625  123, https://doi.org/10.5670/oceanog.2012.46, 2012.

626  Jolliffe, I. T.: Principal Component Analysis, Springer New York, New York, NY,
627  https://doi.org/10.1007/978-1-4757-1904-8, 1986.

628  Kelly, S. M.: The Vertical Mode Decomposition of Surface and Internal Tides in the Presence of a Free

Code de champ modifié

26

Surface and Arbitrary Topography, Journal of Physical Oceanography, 46, 3777–3788, https://doi.org/10.1175/JPO-D-16-0131.1, 2016.

Le Guillou, F., Lahaye, N., Ubelmann, C., Metref, S., Cosme, E., Ponte, A.: Joint estimation of balanced motions and internal tides from future wide-swath altimetry. Journal of Advances in Modeling Earth Systems, 13(12), e2021MS002613. https://doi.org/10.1029/2021ms002613, 2021.

Le Provost, C.: Chapter 6 Ocean Tides, in: International Geophysics, vol. 69, Elsevier, 267–303, https://doi.org/10.1016/S0074-6142(01)80151-0, 2001.

Lentini, C., Magalhães, J., Da Silva, J., and Lorenzzetti, J.: Transcritical Flow and Generation of Internal Solitary Waves off the Amazon River: Synthetic Aperture Radar Observations and Interpretation, Oceanog., 29, 187–195, https://doi.org/10.5670/oceanog.2016.88, 2016.

Lyard, F. H., Allain, D. J., Cancet, M., Carrere, L., and Picot, N.: FES2014 global ocean tide atlas: design and performance, Ocean Sci., 17, 615–649, https://doi.org/10.5194/os-17-615-2021, 2021.

Magalhaes, J. M., Da Silva, J. C. B., Buijsman, M. C., and Garcia, C. A. E.: Effect of the North Equatorial Counter Current on the generation and propagation of internal solitary waves off the Amazon shelf (SAR observations), Ocean Sci., 12, 243–255, https://doi.org/10.5194/os-12-243-2016, 2016.

Morrow, R., Fu, L.-L., Ardhuin, F., Benkiran, M., Chapron, B., Cosme, E., d'Ovidio, F., Farrar, J. T., Gille, S. T., Lapeyre, G., Le Traon, P.-Y., Pascual, A., Ponte, A., Qiu, B., Rascle, N., Ubelmann, C., Wang, J., and Zaron, E. D.: Global Observations of Fine-Scale Ocean Surface Topography With the Surface Water and Ocean Topography (SWOT) Mission, Front. Mar. Sci., 6, 232, https://doi.org/10.3389/fmars.2019.00232, 2019.

Nash, J., Shroyer, E., Kelly, S., Inall, M., Duda, T., Levine, M., Jones, N., and Musgrave, R.: Are Any Coastal Internal Tides Predictable?, oceanog, 25, 80–95, https://doi.org/10.5670/oceanog.2012.44, 2012.

Nelson, A. D., Arbic, B. K., Zaron, E. D., Savage, A. C., Richman, J. G., Buijsman, M. C., and Shriver, J. F.: Toward Realistic Nonstationarity of Semidiurnal Baroclinic Tides in a Hydrodynamic Model, JGR Oceans, 124, 6632–6642, https://doi.org/10.1029/2018JC014737, 2019.

Niwa, Y. and Hibiya, T.: Estimation of baroclinic tide energy available for deep ocean mixing based on three-dimensional global numerical simulations, J Oceanogr, 67, 493–502, https://doi.org/10.1007/s10872-011-0052-1, 2011.

Ponte, A. L. and Klein, P.: Incoherent signature of internal tides on sea level in idealized numerical simulations, Geophysical Research Letters, 42, 1520–1526, https://doi.org/10.1002/2014GL062583, 2015.

Ray, R. D. and Mitchum, G. T.: Surface manifestation of internal tides in the deep ocean: observations from altimetry and island gauges, Progress in Oceanography, 40, 135–162, https://doi.org/10.1016/S0079-6611(97)00025-6, 1997.

Savage, A. C., Waterhouse, A. F., and Kelly, S. M.: Internal Tide Nonstationarity and Wave–Mesoscale Interactions in the Tasman Sea, Journal of Physical Oceanography, 50, 2931–2951, https://doi.org/10.1175/JPO-D-19-0283.1, 2020.

Solano, M. S., Buijsman, M. C., Shriver, J. F., Magalhaes, J., Da Silva, J., Jackson, C., Arbic, B. K., and Barkan, R.: Nonlinear Internal Tides in a Realistically Forced Global Ocean Simulation, JGR Oceans, 128,

669     e2023JC019913, https://doi.org/10.1029/2023JC019913, 2023.

670     St. Laurent, L. and Garrett, C.: The Role of Internal Tides in Mixing the Deep Ocean, J. Phys. Oceanogr.,
671     32, 2882–2899, https://doi.org/10.1175/1520-0485(2002)032<2882:TROITI>2.0.CO;2, 2002.

672     Takahashi, K., Montecinos, A., Goubanova, K., and Dewitte, B.: ENSO regimes: Reinterpreting the
673     canonical and Modoki El Niño: REINTERPRETING ENSO MODES, Geophys. Res. Lett., 38, n/a-n/a,
674     https://doi.org/10.1029/2011GL047364, 2011.

675     Tchilibou, M., Gourdeau, L., Lyard, F., Morrow, R., Koch Larrouy, A., Allain, D., and Djath, B.: Internal
676     tides in the Solomon Sea in contrasted ENSO conditions, Ocean Sci., 16, 615–635,
677     https://doi.org/10.5194/os-16-615-2020, 2020.

678     Tchilibou, M., Koch-Larrouy, A., Barbot, S., Lyard, F., Morel, Y., Jouanno, J., and Morrow, R.: Internal
679     tides off the Amazon shelf during two contrasted seasons: interactions with background circulation
680     and SSH imprints, Ocean Sci., 18, 1591–1618, https://doi.org/10.5194/os-18-1591-2022, 2022.

681     Ubelmann, C., Dibarboure, G., Gaultier, L., Ponte, A., Ardhuin, F., Ballarotta, M., and Faugère, Y.:
682     Reconstructing Ocean Surface Current Combining Altimetry and Future Spaceborne Doppler Data, JGR
683     Oceans, 126, e2020JC016560, https://doi.org/10.1029/2020JC016560, 2021.

684     Ubelmann, C., Carrere, L., Durand, C., Dibarboure, G., Faugère, Y., Ballarotta, M., Briol, F., and Lyard,
685     F.: Simultaneous estimation of ocean mesoscale and coherent internal tide sea surface height
686     signatures from the global altimetry record, Ocean Sci., 18, 469–481, https://doi.org/10.5194/os-18-
687     469-2022, 2022.

688     Ubelmann, C., P. Klein, and L.-L. Fu: Dynamic interpolation of sea surface height and potential
689     applications for future high-resolution altimetry mapping. J. Atmos. Ocean. Technol., 32, 177–184,
690     https://doi.org/10.1175/JTECH-D-14-00152.1, 2015

691     Vic, C., Naveira Garabato, A. C., Green, J. A. M., Waterhouse, A. F., Zhao, Z., Melet, A., De Lavergne, C.,
692     Buijsman, M. C., and Stephenson, G. R.: Deep-ocean mixing driven by small-scale internal tides, Nat
693     Commun, 10, 2099, https://doi.org/10.1038/s41467-019-10149-5, 2019.

694     Wang, H., Grisouard, N., Salehipour, H., Nuz, A., Poon, M., & Ponte, A. L.: A deep learning approach
695     to extract internal tides scattered by geostrophic turbulence. Geophysical Research
696     Letters, 49, e2022GL099400. https://doi.org/10.1029/2022GL099400, 2022.

697     Wang, J. and Fu, L.-L.: On the Long-Wavelength Validation of the SWOT KaRIn Measurement, Journal
698     of Atmospheric and Oceanic Technology, 36, 843–848, https://doi.org/10.1175/JTECH-D-18-0148.1,
699     2019.

700     Zaron E. D. and S. Elipot: Estimates of Baroclinic Tidal Sea Level and Currents from Lagrangian Drifters
701     and Satellite Altimetry, Journal of Atmospheric and Oceanic Technology, 41, 781-802
702     https://doi.org/10.1175/JTECH-D-23-0159.1, 2024.

703     Zaron, E. D.: Mapping the nonstationary internal tide with satellite altimetry, JGR Oceans, 122, 539–
704     554, https://doi.org/10.1002/2016JC012487, 2017.

705     Zaron, E. D.: Baroclinic Tidal Sea Level from Exact-Repeat Mission Altimetry, Journal of Physical
706     Oceanography, 49, 193–210, https://doi.org/10.1175/JPO-D-18-0127.1, 2019.

707     Zaron, E. D. and Ray, R. D.: Aliased Tidal Variability in Mesoscale Sea Level Anomaly Maps, Journal of

Code de champ modifié

Code de champ modifié

708  Atmospheric and Oceanic Technology, 35, 2421–2435, https://doi.org/10.1175/JTECH-D-18-0089.1,
709  2018.

710  Zhao, Z.: Mapping Internal Tides from Satellite Altimetry Without Blind Directions, JGR Oceans, 124,
711  8605–8625, https://doi.org/10.1029/2019JC015507, 2019.

712  Zhao, Z.: Seasonal mode-1 M2 internal tides from satellite altimetry, Journal of Physical Oceanography,
713  https://doi.org/10.1175/JPO-D-21-0001.1, 2021.

714  Zhou, X., Wang, D., and Chen, D.: Validating satellite altimeter measurements of internal tides with
715  long-term TAO/TRITON buoy observations at 2°S–156°E, Geophysical Research Letters, 42, 4040–4046,
716  https://doi.org/10.1002/2015GL063669, 2015.

717

718

719

720

721

722

723

724

725

726